PHYSICAL REVIEW E **67**, 051706 (2003)

Dynamic local-layer response of surface-stabilized ferroelectric liquid crystals to a high electric field by time-resolved x-ray microdiffraction

Yumiko Takahashi*
The Graduate University for Advanced Studies, 1-1 Oho Tsukuba, Ibaraki 305-0801, Japan

Atsuo Iida
Photon Factory, Institute of Materials Structure Science, High Energy Accelerator Research Organization, 1-1 Oho Tsukuba, Ibaraki 305-0801, Japan

Yoichi Takanishi, Toyokazu Ogasawara, Michi Nakata, Ken Ishikawa, and Hideo Takezoe
Department of Organic and Polymeric Materials, Tokyo Institute of Technology, O-okayama Meguro-ku, Tokyo 152-8552, Japan

(Received 15 August 2002; revised manuscript received 20 February 2003; published 23 May 2003)

Time-resolved synchrotron x-ray microdiffraction measurements have directly revealed the dynamic local-layer response to the high electric field in a surface-stabilized ferroelectric liquid crystal. The irreversible layer transformation under the increasing electric field is found to consist of two stages; the initial vertical chevron structure transforms to the alternate vertical and horizontal chevrons and, with increasing field, the chevron angle decreases and the horizontal chevron structure develops. The time-resolved microdiffraction measurement has clarified the detailed reversible layer transformation between the mostly horizontal chevron at the high field and the so-called quasibookshelf at the low field during the ac field application. The transient layer response time is about 0.1–0.2 and 0.3–0.4 ms for falling and rising edges, respectively, and is slightly longer than the optical response time. The layer transformation is discussed in terms of electric torque and surface anchoring. The local-layer response in the antiferroelectric liquid crystal is also discussed for comparison.

DOI: 10.1103/PhysRevE.67.051706 PACS number(s): 61.30.−v

I. INTRODUCTION

The local-layer structures of ferroelectric liquid crystals (FLCs) and antiferroelectric liquid crystals (AFLCs) and their layer response to an electric field have attracted much attention both from display device applications and fundamental physics [1,2]. When the smectic-*A* (Sm*A*) phase is cooled down to the chiral smectic-*C* (Sm*C**) phase, the reduction of the layer spacing is compensated by a vertical chevron (v-chevron) structure in a surface-stabilized cell [2–7]. Optical and electro-optical phenomena could be interpreted in terms of this v-chevron structure and its modification. Under the high electric field, an irreversible layer transition from the initial v chevron to the so-called quasibookshelf structure was observed in both surface-stabilized AFLC and FLC cells [9–11]. When observed with a polarized optical microscope, the quasibookshelf structure often accompanies the stripe texture that degrades the optical contrast for display applications. The stripe texture has been discussed with regard to the horizontal chevron (h-chevron) structure [12]. The h chevron is realized due to the interaction between the applied electric field and the spontaneous polarization of the molecule. The h-chevron structures, however, are not restricted to the Sm*C** under the high-field treatment, but also they were found in the FLC without the field treatment [13] and in the electroclinic effect in the Sm*A* phase [12,14,15]. Recently, the v chevron to quasibookshelf transition has been also studied in detail by x-ray small angle scattering in relation to the ferroelectric, ferrielectric, and antiferroelectric phases as a function of temperature and the electric field [16–19]. Since the h chevron is a laterally inhomogeneous layer structure in a cell, a spatially resolved x-ray technique is indispensable to directly determine the local-layer structure. Small angle x-ray scattering with a synchrotron x-ray microbeam is the direct microscopic technique and has proven to be quite effective for the characterization of smectic liquid crystals [20–25].

Obviously, for the study of the electro-optical behavior of the FLCs and AFLCs, it is important to directly investigate the dynamic as well as the static layer structure of the v and h chevrons in detail. The x-ray experiments having a millisecond (ms) to microsecond (μs) time resolution for the liquid crystal layer determination, however, have been limited in number. The layer responses from a few tens of microseconds to sub-milliseconds were observed even under the relatively low electric field of a symmetric bipolar pulse [26,27]. Recently, the local-layer structure in the AFLCs and its response to the applied electric field were successfully revealed by time-resolved synchrotron x-ray microdiffraction [28,29].

In this paper, the local-layer structure of the FLCs and its response to the electric field are investigated to reveal the dynamic interaction of the field with the local-layer structure by x-ray small angle scattering with a few μm spatial resolution and a few tens of μs time resolution. Furthermore, the orthogonal ω- and χ-angular dependences of diffracted intensities are fully utilized to study the field-induced layer transformation. Simultaneous observation of the optical response with the x-ray measurement also makes it possible to discuss the relationship between the molecular and the layer re-

---

*Present address: Nihon University, Surugadai, Kanda, Chiyoda-ku, Tokyo 101-8308, Japan.

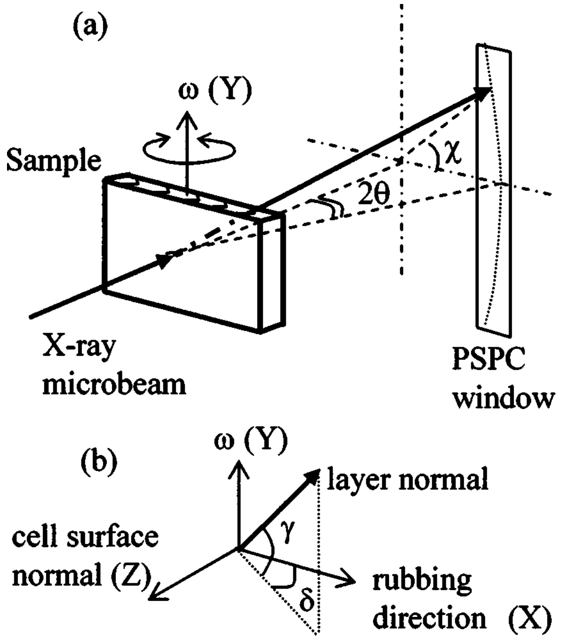

FIG. 1. (a) Experimental setup for synchrotron x-ray microbeam diffraction. (b) Sample coordinates for the smectic layer normal. The angle δ is the tilt angle or the vertical chevron angle. γ is the in-plane deflection angle or the horizontal chevron angle when the chevron structure is periodic.

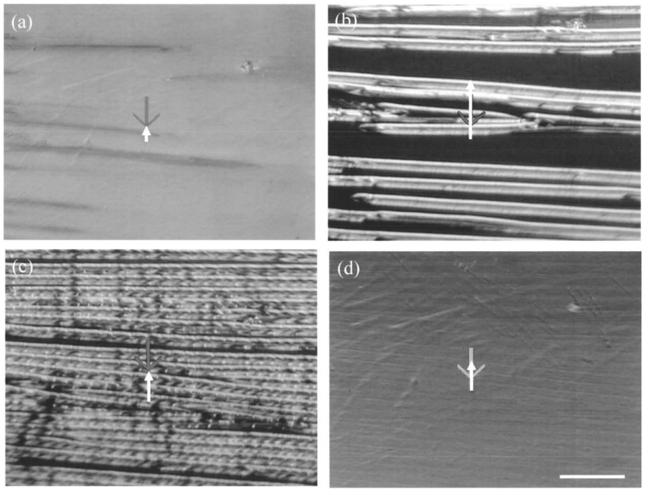

FIG. 2. Polarized optical micrographs of textures of the initial stage before field application (a), ±18 V (b), ±28 V (c), and ±60 V (d) under the triangular wave form (5 Hz). The sample was TK-C101. The cell thickness was about 7.5 μm. The measurement was done at room temperature. The rubbing direction was set horizontally. White arrows show the direction and the region of the x-ray measurement shown in Fig. 3. A scale mark is 100 μm. (Weak gray arrows show points of measurements during the experiments.)

sponse. The quasistatic and transient layer transformations for the triangular-form and the step-form electric fields, respectively, are reported. The results are also discussed in relation to the AFLC layer response.

II. EXPERIMENT

The sample was TK-C101 (Chisso) [23] sandwiched between ITO-coated glass plates (150 μm thick) rubbed on one side after coating a polyimide alignment film. The phase sequence of TK-C101 is iso(80 °C) N^*(70 °C)SmA(56 °C)SmC^*. The experiments were performed in the SmC^* phase at room temperature. Most of the experiments were carried out with one-side rubbing cells, which is the same alignment condition as previous AFLC experiments [28,29]. The cell gap was about 5–8 μm. For comparison, an AFLC sample (S)-TFMHPOBC [4-(1-trifluoromethyl heptyloxycarbonyl)phenyl 4′-octyloxybiphenyl-4-carboxylate] was also measured at the same sample temperature of $T_c - 10°$ as previous experiments [28,29], where T_c is the phase transition temperature from SmA to SmC_A^* (109 °C).

The x-ray diffraction experiments were carried out on beam line 4A at the Photon Factory (PF). The experimental detail has been already reported in the previous paper [28], so only a brief description is given here. The beam size was about 3(h)×4(v) μm^2 and the angular divergence of the incident beam was about 1.0 mrad both in the horizontal and in the vertical direction. The incident x-ray energy was 8 keV (1.55 Å). The diffraction geometry is schematically shown in Fig. 1(a). The rubbing direction was set horizontally. The χ-intensity distribution (χ profile) on a position sensitive proportional counter was collected simultaneously. The ω-scan intensity profile (ω profile) was obtained by rotating the sample around a vertical axis (Y). The ω intensity is the integrated intensity with respect to χ in the present paper. No absorption correction for the cell glass plates was made. The layer deflection angles δ and γ are defined in Fig. 1(b).

The optical response was obtained by a photomultiplier attached to an *in situ* polarized microscope during the x-ray measurement, though the optical measurement area was about 100 μm in diameter and was much larger than the x-ray microbeam size.

A triangular-form (5 Hz, $\pm 1 - \pm 65$ V) or a step-form (25–100 Hz, $\pm 45 - \pm 65$ V) electric field was applied to the sample. The time-resolved ω profile and χ profile were obtained with an MCS (multichannel scaler) mode and a gated MCA (multichannel analyzer) mode, respectively. A minimum dwell time for the MCS mode was 10 μs. In the gated MCA mode, the χ profiles at eight sampling points in one cycle of the applied field were collected with a minimum time resolution of 10 μs. MCS and MCA data were summed within a measurement time.

III. RESULTS

A. Time integrated spatial distribution of the diffraction profile

The time integrated spatial distribution of the x-ray diffraction profile from TK-C101 was measured as a function of an applied voltage (Fig. 3) together with the *in situ* observation of the texture by a polarized optical microscope (Fig. 2).

Figures 3(1-a) and 3(1-b) show series of ω and χ profiles, respectively, across the narrow wall at an initial state before the field application. The v-chevron structure (peaks at $\omega = \pm 21°$) is clearly seen in Fig. 3(1-a). The peaks that ap-

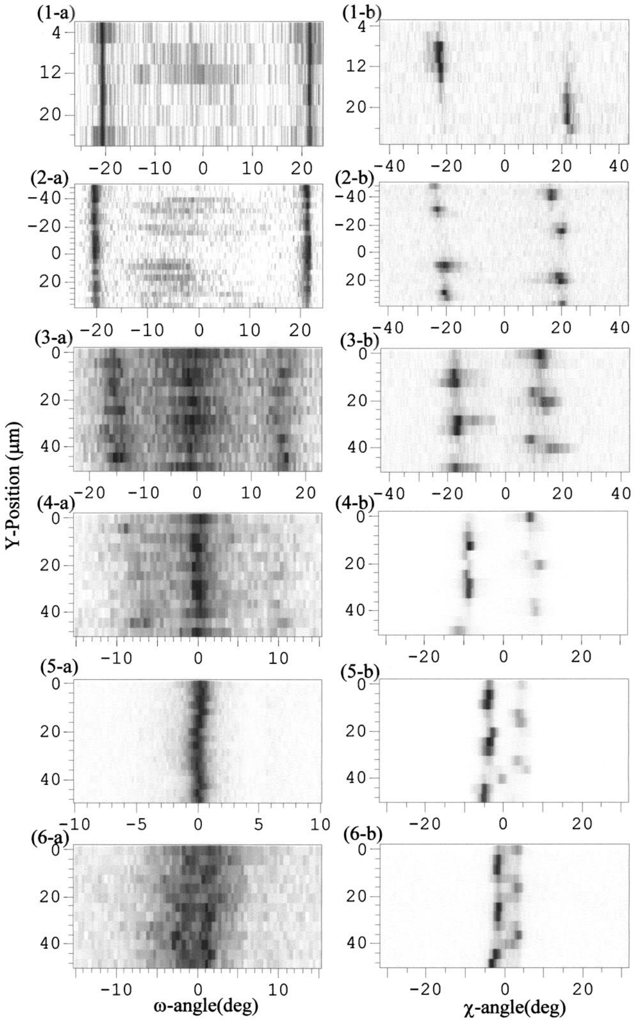

FIG. 3. Series of ω profiles (a) and χ profiles (b) as a function of the vertical position (Y direction). (1-a) and (1-b) were obtained before the field application. (2-a) and (2-b), (3-a) and (3-b), (4-a) and (4-b), and (5-a) and (5-b) were obtained during the triangular field of ±18, ±30, ±40, and ±60 V, respectively. (6-a) and (6-b) were obtained after turning off the field. The χ profiles were obtained at $\omega = 0°$ except for (2-b) where $\omega = -5.8°$ (see text). The scanning step in the Y direction was 4 μm. The darker part corresponds to the higher diffracted intensity. X-ray intensities were normalized by the highest intensity in each figure.

peared in χ profiles [Fig. 3(1-b)] are due to a pair of the narrow wall of a zigzag defect observed in Fig. 2(a). Thus, the v-chevron angle (δ) and the in-plane deflection angle at the narrow wall (γ) are 21° and 22°, respectively.

When the triangular electric field with a frequency of 5 Hz was applied to the sample, most of the narrow walls in the view field disappeared up to ±5 V [8] and the new line defect (needle defect [20,23], hereafter) appeared above ±10 V. The needle defect usually appeared from a broad wall, the tip of a narrow wall or a spacer edge. At ±18 V [Fig. 2(b)], the needle defect develops and the so-called stripe texture is formed. A series of the ω profiles [Fig. 3(2-a)] shows broad but weak peaks (ω-bookshelf components, hereafter) between the v-chevron peaks. The χ-intensity distribution [Fig. 3(2-b)] obtained at $\omega = -5.8°$ (peak of ω-bookshelf component) shows the alternate intensity variation between the low and high angles indicating the nearly periodic needle-defect formation (h-chevron growth). The angles δ and γ are almost the same as in the initial state.

By increasing the applied voltage, the needle defect further develops and covers the whole area as shown in Fig. 2(c). It is also noted that dense focal conics appear in the needle defect (or stripe) reflecting the strain field. The intensity modulation in Figs. 3(3-a) and 3(3-b) is about 8–10 μm in period, which is close to the cell thickness. Above the applied voltage of around ±30 V, the spatial period of the χ-profile modulation is almost unchanged. The angles δ and γ become small and the FWHM (full width at half maximum) of the v-chevron peak in the ω profile slightly increases up to 1° from the initial one (about 0.4°) indicating the strain introduction.

Up to ±50 V, the stripe texture progressively covers the whole sample area and the focal conics density increases. With increasing applied voltage, the angles δ and γ become small and the v-chevron intensity further becomes weak as shown in Figs. 3(4-a) and 3(4-b). It is noted, however, that the v-chevron structure still remains at this stage.

Above ±50 V, the contrast of the stripe texture becomes very weak and focal conics disappear [Fig. 2(d)]. The ω profiles obtained at ±60 V [Fig. 3(5-a)], which is the highest applied voltage for this sample show a sharp peak near $\omega = 0°$ and are almost independent of the position. The χ profiles [Fig. 3(5-b)], however, show the alternate intensity distribution from position to position. The angle γ decreases down to 5° on an average.

When the electric field is turned off, the ω profile becomes broad and the angle γ becomes small (3°) as shown in Figs. 3(6-a) and 3(6-b). Compared to the initial state, the local-layer structure is irreversibly transformed. The ω profile looks like the quasibookshelf or the strongly modified v-chevron structure.

A series of time integrated spatial distributions in Fig. 3 has revealed the local-layer structure in a microscopic scale. The detail of the layer structure, however, seems to depend on the sample and the history of the field application. Figure 4 shows the other typical ω and χ profiles from a different sample for the high applied field [Figs. 4(a) and 4(b)] and after turning off the field [Figs. 4(c) and 4(d)]. The ω profiles at the high voltage (±50 V) show the single peak [Fig. 4(a)] similar to Fig. 3(5-a), while the χ profiles in Fig. 4(b) are broader than those in Fig. 3(5-b) and the periodic structure is not so clear. After turning off the field, this type of the sample shows a single peak in the χ profile [Fig. 4(d)] in contrast to the alternate two peaks shown in Fig. 3(6-b), while the ω profile [Fig. 4(c)] is similar to Fig. 3(6-a). For all these differences among samples, the local-layer structure after turning off the field is characterized by the broadening of the ω profile and the narrowing of the chevron angle γ or a single peak in the χ profile. Hereafter, the layer structures in Figs. 3 and 4 are referred to as the type D and type S, indicating the double and single peaks in the χ profile after turning off the field, respectively.

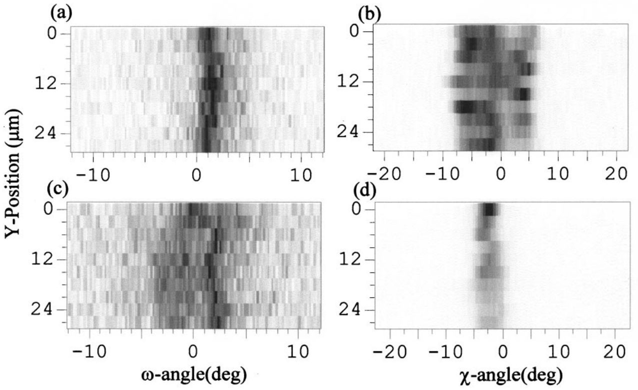

FIG. 4. Series of ω profiles [(a) and (c)] and χ profiles at $\omega = 0°$ [(b) and (c)] as a function of the vertical position across the stripe. Under the ±50 V field application [(a) and (b)] and after turning off the field [(c) and (d)]. The sample thickness was 6 μm.

To summarize the layer deformation process, the ω and χ profiles in Fig. 3 are summed for *Y* positions (temporally and spatially integrated profiles, Fig. 5). The irreversible v chevron to the quasibookshelf transformation in ω profiles [Fig. 5(a)] well agrees with previous x-ray diffraction experiments [8,10,17,19], while the simultaneous χ-profile measurement clearly indicates various stages of the h-chevron formation.

Finally, the layer transformation having a long relaxation time is mentioned. Uppermost profiles in Fig. 5 (long) are obtained after a long time interval (about four months) without electric field application. Poor statistics are due to the lack of the spatial integration in this case. Multiple broad peaks in the ω profile indicate the partial recovery of the v-chevron structure. The layer relaxation seems to proceed quite slowly.

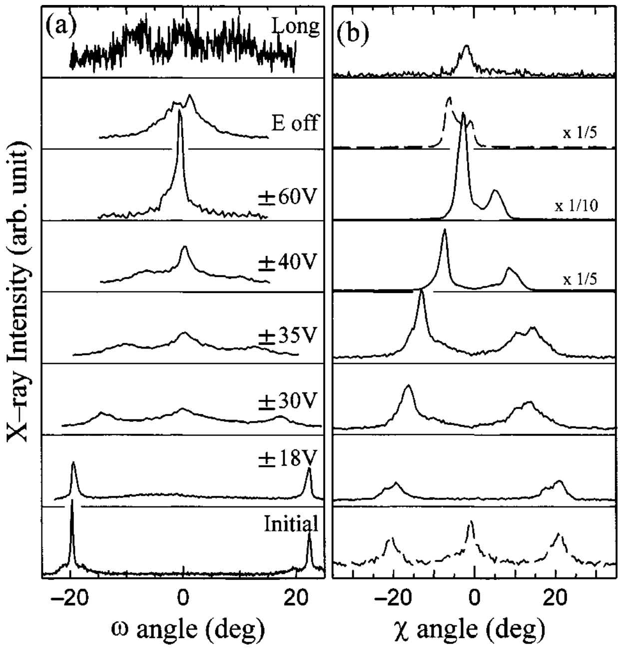

FIG. 5. Summary of the time integrated ω profile (a) and χ profile (b). From ±18 V to *E* off (after turning off the electric field), the diffracted intensities were obtained by integrating over the position from series of ω and χ profiles (Fig. 3). For the initial profile, the χ profile (broken line) was measured during the ω-profile measurement at the center of the narrow wall (integrated over ω angle). Uppermost profiles (long) were obtained from a different sample at a single position (no spatial integration) after a long interval without electric field application.

B. Quasistatic response

The time-resolved experiments under the quasistatic condition were performed with a 5-Hz triangular wave for the sample after the irreversible transition, i.e., time-resolved measurements of Figs. 3(5-a) and 3(5-b). Figures 6(a) and 6(b) show the time-resolved MCS-mode ω profiles from the sample used in Fig. 3 for one cycle of applied voltage (±60 V amplitude) as a function of time for different positions (8-μm apart in the *Y* position). In Fig. 6(a), a single peak near $\omega = 0°$ at the high field shifts to the low angle by about 1° and becomes broad at the low field. In Fig. 6(b), a weak hump appears at the low angle side and it shifts to lower angles with increasing voltage, and the broad double peak appears at low voltage. These two patterns, Figs. 6(a) and 6(b), appeared from position to position in the *Y* direction alternately. Figure 6(c) shows the ω-profile intensity near $\omega = 0°$ obtained from Fig. 6(b) as a function of the applied voltage (voltage-dependent profile). The intensity has maxima at around ±30 V and decreases at lower and higher applied voltages. The decrease in the intensity is compensated by the low-angle weak hump at the high field, while, naturally, it is due to the shift and broadening of the ω-profile peak at the low field. The layer response is different from the optical one.

Although Figs. 6(a) and 6(b) are the typical time-resolved ω profiles for the triangular wave, several types of the ω profile seem to appear at the low field from various samples and positions: the asymmetric broad peak [tilted bent bookshelf, Fig. 6(a)], the broad double peak [modified v chevron, Fig. 6(b)] and the symmetric broad peak (quasibookshelf). The common feature of these is the broad profile. It is also noted that the FWHM of the ω profile after turning off the field [Fig. 3(6-a)] is broader than that at 0 V during the ac field application. Therefore, the layer response under the triangular field (5 Hz) is a quasistatic process.

The time-resolved MCA-mode χ profile shows remarkable profile change during the field application. Figures 7(a) and 7(b) are obtained from different samples. In Fig. 7(a), the angular separation of about 10° of the double peak at the high field ($\gamma \sim 5°$) decreases down to 4°–5° at the low field ($\gamma \sim 2°$) while, in Fig. 7(b), the double peak at the high field changes continuously to the single peak at the low field. Figures 7(a) and 7(b) relate to the type *D* and type *S* layer transformations, respectively. In practice, the time dependence of the type *S* [Fig. 7(b)] is more frequently observed. The positional dependence of the time-resolved χ profile showed the alternate low- and high-angle peaks.

The reversible layer response such as shown in Figs. 6 and 7 started when δ and/or γ became less than ~10° or dense focal conics disappeared. Below that voltage, no con-

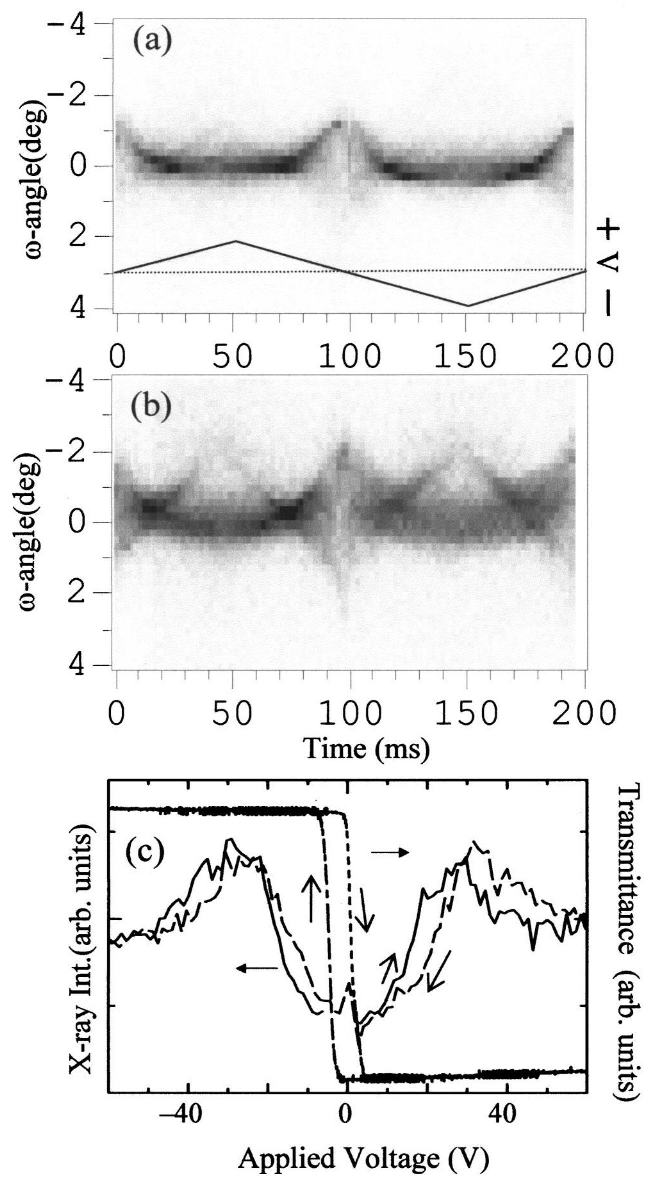

FIG. 6. Time-resolved MCS-mode ω profiles for one cycle of the triangular wave form (5 Hz) [(a) and (b)]. (a) and (b) were obtained from the sample used in Fig. 3 at positions 8 μm apart in the Y direction. An inset in (a) shows the wave form applied to the sample. The maximum applied voltage was ±60 V. The time resolution was 1 ms. The data for the last 2.5% of one cycle are lacking due to the limitation of the timing control procedure for present electronics. (c) The applied voltage dependence of the ω-profile intensity near $\omega = 0°$ (voltage-dependence profile) obtained from (b). The optical transmittance is also shown.

spicuous χ-profile response to the applied field was observed.

From the time-resolved measurement, the quasistatic reversible layer transformation was revealed for the first time.

C. Transient response

The transient layer response was investigated under a step-form electric field (25 Hz, ±60 V). The time-resolved MCS-mode ω profile for one cycle of the field is shown in Fig. 8(a). The ω profiles at the high and low fields, time integrated for 3 ms of Fig. 8(a), are shown in Fig. 8(b). A strong peak near $\omega = 0°$ and weak humps near $\omega = \pm 4°$ at the high field, and a broad single peak at the low field are seen. The time dependent integrated intensity of the ω profile [integrated Fig. 8(a) from $\omega = -0.6°$ to $\omega = 1.6°$] shown in Fig. 8(c) remains nearly constant at the high field, while that at the zero-voltage region shows the slow fluctuation, up to a few milliseconds after the field change. The corresponding optical response in Fig. 8(c) shows the memory effect when the electric field is turned off (+60–0 V, falling edge) and the sharp decrease when the field is turned on (0–60 V, rising edge). Figures 9(a) and 9(b) show the detailed intensity variation at $\omega = 0°$ and 0.4° at the falling edge and the rising edge, respectively. At the falling edge, the decrease of the ω-profile intensity depends on the ω angle, while at the rising edge the intensity increase seems to be independent of the ω angle. The transient time in the time-resolved ω profile, when it is defined by the time interval during which the ω intensity in Fig. 9 levels off after the electric field change, is ca. 0.2–0.4 ms for the falling edge and about 0.5 ms for the rising edge. The optical transient time is about 30 μs at the rising edge for this sample [Fig. 8(c)] and usually less than 0.1 ms; it is shorter than the layer transient time.

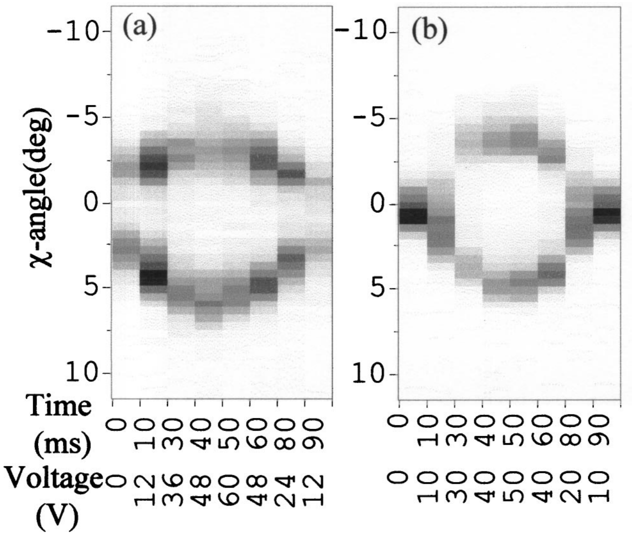

FIG. 7. Time-resolved MCA-mode χ profiles for a half cycle of the triangular wave form [5 Hz, see the inset of Fig. 6(a)]. (a) and (b) were obtained for different samples and the maximum applied voltages were ±60 and ±50 V, respectively. Both profiles were obtained near $\omega \sim 0°$. 10 ms time resolution. Note that the sampling times (abscissa) are not at equal intervals.

The time-resolved χ profiles for falling edge and rising edge are shown in Figs. 10(a) and 10(b), respectively. The time-resolved χ profiles have the double peak and the single peak at the high and the low voltage, respectively, and they correspond well to the quasistatic time-resolved χ profile shown in Fig. 7. The response time in the χ profile, during which the major profile change occurs after the applied field change, is 0.1–0.2 and 0.3–0.4 ms for the falling edge and the rising edge, respectively. The response time for the χ profile is slightly shorter than the transient time for the ω

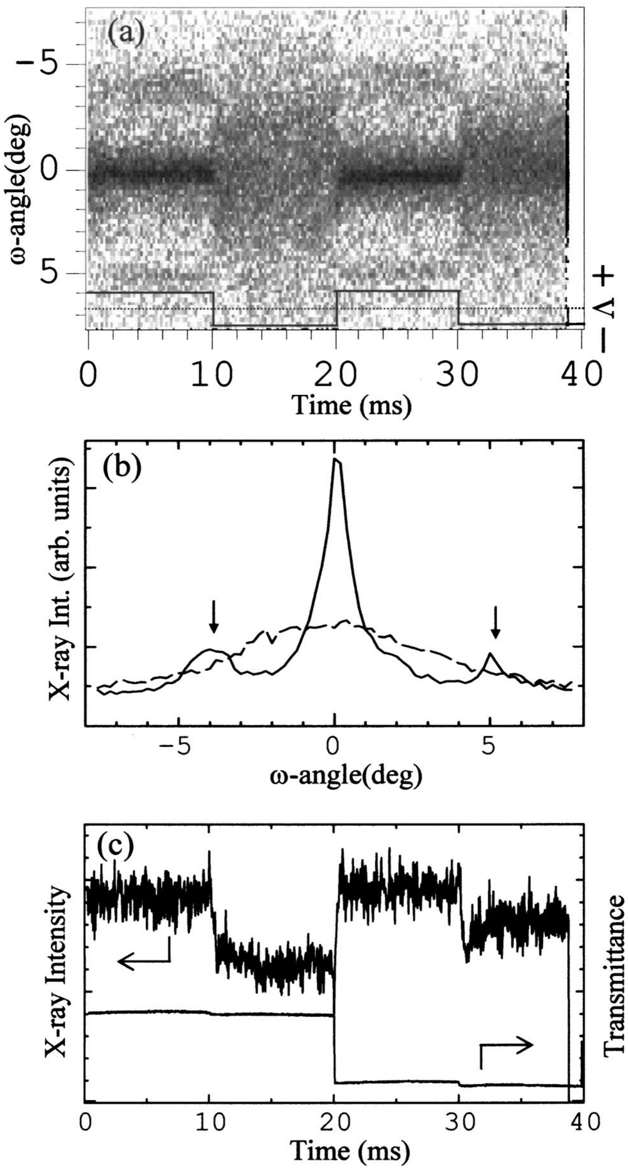

FIG. 8. (a) Time-resolved MCS-mode ω profiles for the step-form electric field (25 Hz, ±60 V). 0.04 ms time resolution. An inset shows the wave form applied to the sample. (b) ω profiles integrated over 3 ms around 60 V (solid) and 0 V (broken). Arrows show humps that appeared at +60 V applied voltage. (c) The time dependence of the ω-profile integrated intensity around $\omega = 0.2^\circ - 1^\circ$ obtained from (a). An optical transmittance is also shown.

profile. This might be caused by the following reasons; the ω profile is the integrated intensity for the χ angle in the present experiment resulting in the insensitive response, and the marked change in the layer structure is closely related to the h chevron rather than the v chevron (or the layer deformation around the *Y* axis). In practice, the slow intensity variation in the χ profile (more than 1 ms) was observed and it corresponded to the slowly varying part of the ω profile.

D. AFLC response

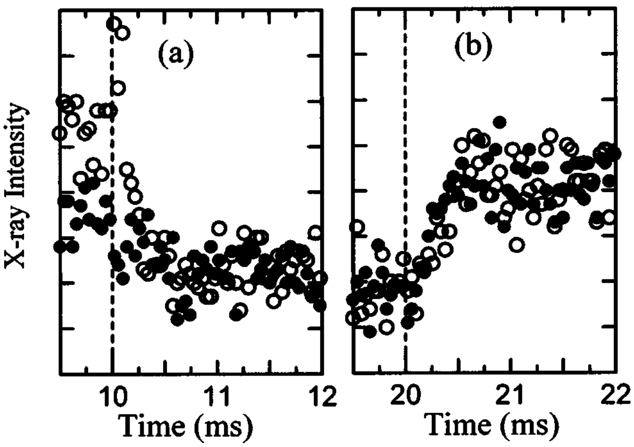

FIG. 9. X-ray intensity near the falling (+60–0 V) (a) and rising (0–−60 V) (b) edges obtained from Fig. 8(a) for $\omega = 0^\circ$ (○) and $\omega = 0.4^\circ$ (●). Dotted lines show the time when the applied field changes.

An AFLC sample TFMHPOBC was also measured with the same technique. At the initial stage before the field application, the sample showed the stripe texture which was a combination of the v and the h chevron [28]. Figure 11 shows the applied voltage dependences of the angles δ and γ for TFMHPOBC together with those for TK-C101. A clear threshold voltage for TFMHPOBC (AFLC) in contrast to the gradual layer change in TK-C101 (FLC) agrees with previous experiments [9,17–19]. It is noted that not only δ but also γ shows the similar voltage dependence. The threshold voltage relates to the onset of the ferroelectric state.

During the reversible layer transformation under the triangular wave form (5 Hz, ±65 V), the time-resolved MCS ω profile [Fig. 12(a)] shows the triple peak at the low field and the single peak at the high field. The corresponding time-resolved χ profile [Fig. 12(c)] shows that the two peaks at the high field (50 and 140 ms), though the low-angle peak (around $\chi \sim -1.5^\circ$) is quite weak in this case, become a

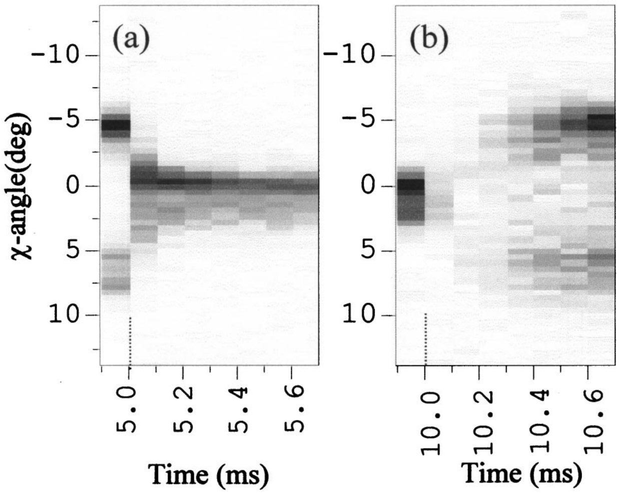

FIG. 10. (a) and (b) are time-resolved MCA-mode χ profiles for the falling edge (+60–0 V) and the rising edge (0–−60 V), respectively, of the step-form electric field (50 Hz, ±60 V); 0.1 ms time resolution. Dotted lines show the time when the applied field changes.

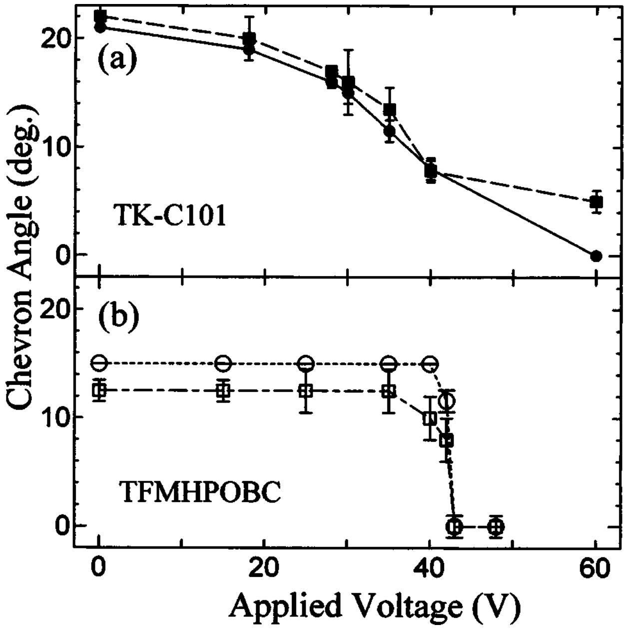

FIG. 11. Applied voltage dependences of the chevron angle δ (■,□) and γ (●,○). (a) and (b) are for TK-C101 (FLC) and TFMHPOBC (AFLC), respectively. The bar shows the FWHM of each peak.

single peak at the medium field (60, 80, and 130 ms) and that the two peaks appear again in the low field (90–110 ms). The angular separation between the two peaks at the low field is wider than that at the high field. From Figs. 12(a) and 12(c), the layer structure is approximately described as the h chevron at the high field, the quasibookshelf at the medium field, and the combination of the h and v chevrons at the low field. Compared to TK-C101 results and the similarity between the optical response and the diffraction intensity [Fig. 12(b)], it was confirmed that the layer structure of TFMHPOBC appearing in the high and medium fields corresponds to the ferroelectric state. The appearance of the low-field h chevron is closely related to the antiferroelectric state due to the field-induced phase transition. It is noted that the x-ray diffraction profile shows the double hysteresis similar to the optical response of AFLCs [2,9], indicating again the important role of layer motion in the electro-optical response.

The transient layer response under the step-form electric field (100 Hz, ±45 V) shows the different behavior between the falling and rising edges. At the falling edge [Figs. 13(a) and 14(a) for ω and χ profiles, respectively], the ferroelectric structure gradually changes to the antiferroelectric one, while at the rising edge [Figs. 13(b) and 14(b)] the layer structure suddenly changes within a present time resolution. The transient time, during which the h chevron of the antiferroelectric and the ferroelectric phases for the falling (T_f) and rising (T_r) edges, respectively, appears after the field change, depends on the sample. Typically, T_f and T_r were 0.1–0.3 and 0.02–0.08 ms, respectively, and corresponded to the slow component of the field-induced phase transition [30]. The quick response of T_r is closely related to the field-induced phase transition. The layer transient time was as fast as the optical response time.

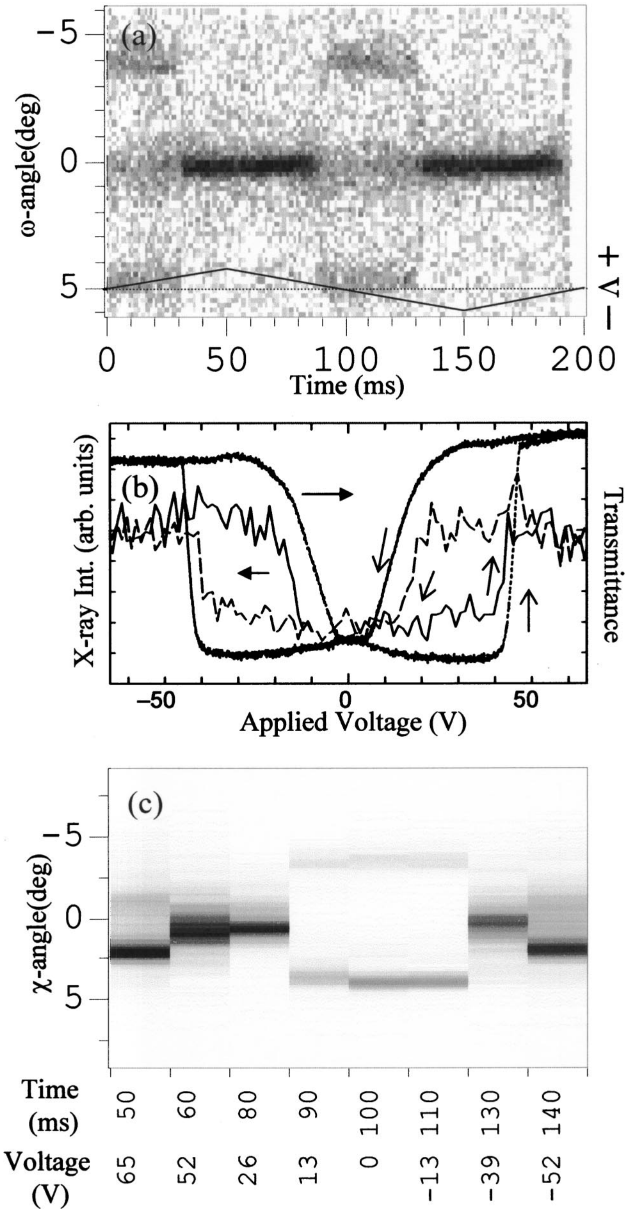

FIG. 12. (a) Time-resolved MCS-mode ω profiles for one cycle of the triangular wave form (5 Hz, ±65 V) for TFMHPOBC. The applied wave form is shown in an inset. 0.5 ms time resolution. (b) The applied voltage dependence of the ω-profile intensity near $\omega = 0°$ (voltage-dependence profile) from (a). The optical transmittance is also shown. (c) Time-resolved MCA-mode χ profiles obtained at $\omega = +0.2°$. 5 ms time resolution. The time from 50 to 150 ms corresponds to the applied voltage from +65 to −65 V. Note that the sampling time (abscissa) is not equal interval. The sample thickness was 5.5 μm.

IV. DISCUSSION

A. Layer structure under the electric field

Since a series of spatially and time-resolved ω- and χ-diffraction profiles was measured, the irreversible and reversible layer transformations of the surface-stabilized FLCs under the electric field can be discussed as shown in Fig. 15.

At the initial state, the layer structure is the v chevron with a zigzag defect [Fig. 15(a)]. The irreversible layer trans-

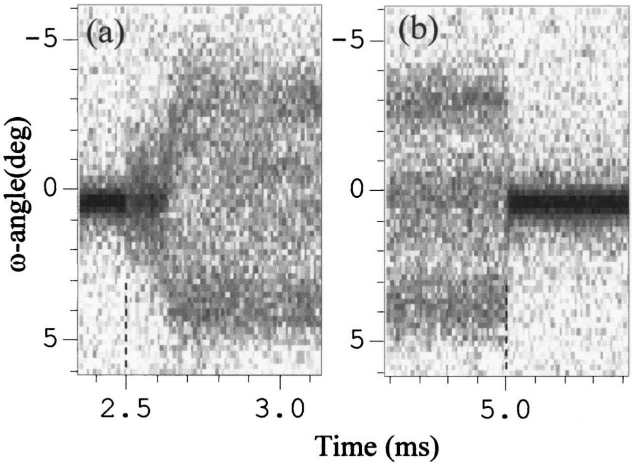

FIG. 13. Time-resolved MCS-mode ω profiles for the step-form electric field (100 Hz, ±45 V) from TFMHPOBC around the falling edge (+45–0 V) (a) and the rising edge (0–−45 V) (b). 10 μs time resolution. Dotted lines show the time when the applied field changes. The sample thickness was about 4 μm.

formation with increasing electric field consists of two stages. When the electric field is first applied to the sample, the electric torque makes the layer upright resulting in the needle-defect generation [Fig. 15(b)]. The in-plane deflection angle γ is nearly equal to the v-chevron angle δ at this stage, though the layer bends along the depth. With an increasing applied voltage, the nearly periodic structure consisting of the alternate v chevron and h chevron is achieved [Fig. 15(c)]. These structures are deduced from the data shown in Figs. 3(1-a,b) and 3(2-a,b) and each layer structure has already been discussed [12,21,22].

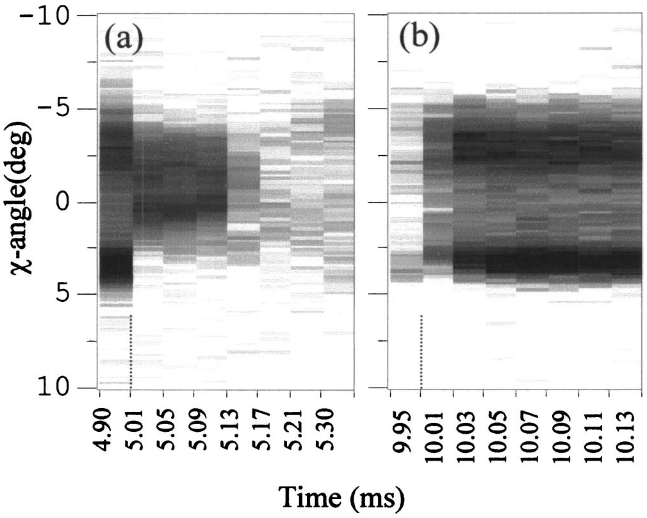

FIG. 14. Time-resolved MCA-mode χ profiles for the step-form electric field (50 Hz, ±45 V) from TFMHPOBC for the falling edge (+45–0 V) (a) and the rising edge (0–−45 V) (b). 40 and 15 μs time resolutions for (a) and (b), respectively. Dotted lines show the time when the applied field changes. Note that the sampling time (abscissa) is not equal interval.

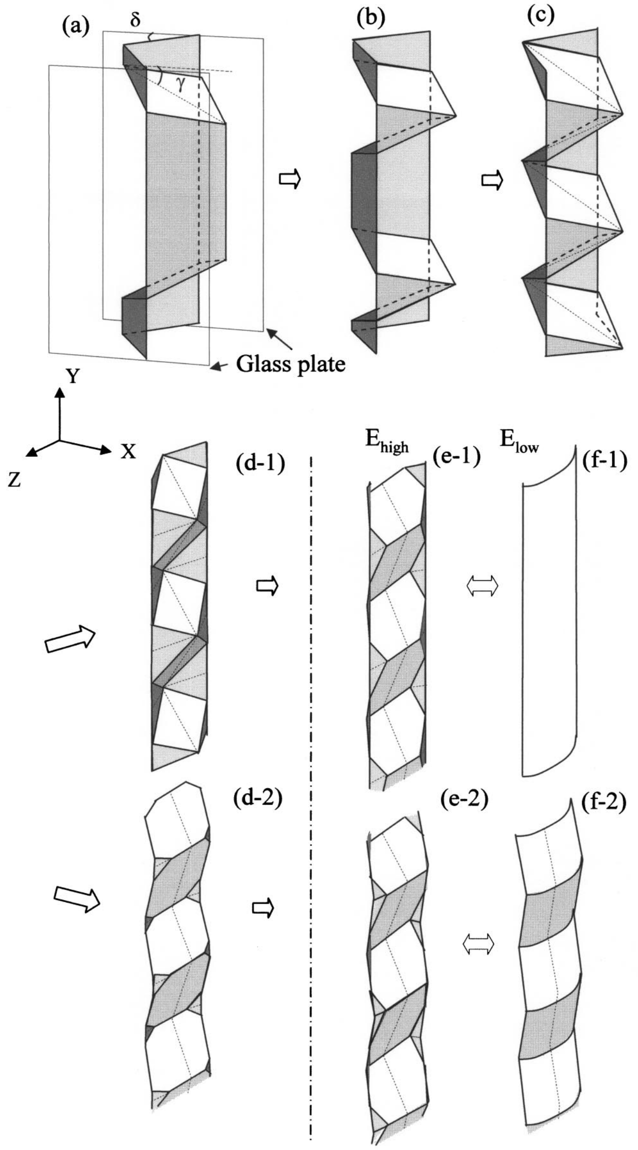

FIG. 15. Schematic representation of the local-layer structure in the FLC cell under the ac electric field. The initial v-chevron structure with narrow walls (a), the generation of the needle defect (b), the development of the needle defect and the formation of the stripe texture (c), and the transformation of the stripe texture (d). The reversible layer transformations are shown in (e) and (f) for the high (E_{high}) and low (E_{low}) electric fields, respectively. (d-1)–(f-1) and (d-2)–(f-2) correspond to the type *S* and type *D* layer transformations (see text). All chevron angles are exaggerated and the layer deformation, especially along the depth, is simplified. Thin dotted lines are a guide for eyes to show the folding direction.

With further increase of the applied voltage, both δ and γ reduce gradually and simultaneously. There are, at least, two types of the surface layer structure: either the layer intersection at the substrate surface is straight [type *S*, Fig. 15(b-1)] or a part of the surface layer is folded [type *D*, Fig. 15(b-2)]. The surface layer of the type *D* has partly changed to the h chevron. The type *S* structure is deduced from Fig. 4, in which the quite broad bookshelf or the deformed v-chevron structure is realized without the h chevron after turning off the field. The single peak at the low voltage in a reversible process in Fig. 7(b) also supports this structure. The type *D* layer structure is inferred from Figs. 3(5-a) and 3(5-b) by considering that the h-chevron area increases to make up the decrease in the v-chevron part. The origin of types *S* and *D* might be due to the difference in the surface treatment and/or the history of the applied field.

The quasistatic reversible layer deformation is illustrated in Figs. 15(e) and 15(f) for the high and low fields, respectively (see Figs. 6 and 7). When the quasibookshelf is realized at the low field (type *S*), the layer bends along the cell depth [Fig. 15(f-1)]. With increasing field, the bulk layer tends to be upright while the surface layer stays almost at the same position, resulting in the appearance of the surface v chevron at the apex of the h chevron, which enables the smooth layer connection [Fig. 15(e-1)]. The v-chevron part corresponds to the small hump appeared in the time-resolved ω profile. When the layer is the deformed h chevron even at the low field (type *D*), the layer response to the electric field is the increase in the h-chevron angle and the appearance of the weak v-chevron component at the high field [Fig. 15(e-2)]. The present results directly show the importance of the substrate surface effect during the h-chevron formation.

After the electric field is turned off, the type *S* structure becomes the broad quasibookshelf or the strongly modified v chevron as seen in Figs. 4(c) and 4(d). For the type *D* structure, the layer is similar to the mostly h-chevron structure shown in Fig. 15(b-2) but with the distortion along the depth.

In Fig. 15, the layer is assumed to be symmetric with respect to the center of the cell for simplicity. In practice, however, the layer might be asymmetric due to the difference in the surface treatment, macroscopically and microscopically, for upper and lower substrates.

B. Origins of the layer deformation

The possible origin of the observed layer deformation is discussed in terms of the electric torque, the substrate surface anchoring, and the molecular orientation. In the following discussion, the conservation of the layer spacing is assumed.

1. Stripe texture formation under electric field

For the generation and the growth of the needle defect, the surface molecule is not necessary to change orientation. Thus, the needle defect is easy to grow [12,24]. With increasing electric field, the angles δ and γ became small simultaneously [Fig. 15(d)] in contrast to the proposed layer structure in which the h chevron grows continuously with increasing applied voltage [12]. The layer spacing along the rubbing direction at the substrate surface *ds* is given by $ds = dc^*/\cos\delta\cos\gamma$, where $dc^* = da\cos\theta$ is the smectic layer spacing, *da* is the molecular length, and θ is the cone angle. At the initial and low-field stages, the angles δ and γ are close to θ indicating $ds \sim da$. The decrease in both δ and γ is the clear and direct evidence of the rearrangement of the surface molecule; thus *ds* reduces. This process is induced by the increasing field-induced torque, which overcomes the surface anchoring. The competition between the electric torque and the surface anchoring induces a strain in the bulk resulting in the appearance of dense focal conics [Fig. 2(c)]. After the new layer structure forms at higher voltages, focal conics disappear. It is noted, however, that the surface molecule does not completely follow the applied field due to the resistive anchoring. Thus the perfect bookshelf structure is seldom observed. Furthermore, surface molecules arrange again after a long interval so that they can become parallel to the rubbing direction slowly (uppermost figure of Fig. 5). Various types of so-called stripe textures are observed after the generation of the needle defect; the layer structure, however, is different among them. The triple peak in the ω profile for the stripe texture obtained with conventional x-ray experiments has been interpreted as the v chevron with the bookshelf at the center of the cell (double-kink structure) [9,17,19]. From the present results, the bookshelf region might be interpreted as a part of the h chevron [Fig. 15(d)] in some cases.

2. Layer structure in the reversible transformation

During the reversible layer transformation process, the layer at the surface is assumed to stay almost at the same position due to the surface anchoring, while the bulk layer (molecule) responds to the applied field under this boundary condition. At the low field, the so-called quasibookshelf structure seems to be realized [Figs. 6, 7, and 15(f)]. The low-field structure, however, is expected to be the v chevron, if constant dc^* is assumed, since the high electric field structure is mainly the h chevron [Fig. 15(e)]. Furthermore, even after turning off the field, the perfect v chevron as seen in the initial state was not observed. The layer structure at the low field is explained as follows. Since the homogeneously bent layer is energetically unfavorable in the smectic phase, the broad peak in the ω profile indicates the introduction of the layer imperfection; i.e., the alignment condition is partly destroyed by the high-field treatment. In other words, as is well known, the good alignment is necessary to realize the v chevron. Even when the macroscopic alignment condition is deteriorated, however, the v chevron may be locally realized at least near the surface to keep the layer spacing constant. From these discussions, the quasibookshelf structure observed at the low field seems to be the imperfect v-chevron structure.

The electric torque makes the layer upright resulting in the h-chevron formation at the high field, whereas the surface anchoring tends to align the v-chevron layer. The difference in the transient layer response between the falling and rising edges observed in Figs. 9 and 10 can be explained by these two forces. At the rising edge, the molecule should overcome the surface anchoring, while the anchoring force alone exists at the falling edge. Thus, in the FLCs, the transient time at the rising edge is slower than that at the falling edge.

Under both triangular- and step-form electric fields, the layer transformed depending on the electric field, while the optical response showed the well-known memory effect [Figs. 6(c) and 8(c)]. In other words, the bulk molecular position moves while the molecular orientation remains nearly the same during the layer deformation. The time-resolved diffraction measurement clarified the molecular motion that was not observed by the optical measurement alone.

V. CONCLUSION

The time-resolved x-ray microdiffraction measurement clarified the local-layer structure response in FLC cells to the electric field. The temporally and spatially resolved ω and χ profiles can offer the information for the reconstruction of the time dependent layer structure, which has been estimated from indirect observations. The initial v-chevron structure changed to the combination of the v chevron and the h chevron at relatively low electric field as the growth of the needle defect. The chevron angles then reduced continuously with increasing electric field. After the irreversible layer transformation, the transition between the h chevron with a small v-chevron part (high field) and the so-called quasibookshelf (low field) occurred reversibly during the ac field application. The low-field quasibookshelf seems to be the imperfect v-chevron structure. The electric torque and the surface anchoring are major driving forces for the reversible layer transformation. Time-resolved measurements also revealed the difference in the response between the local layer and the molecular orientation. The reversible transformation process in the FLC cell corresponds well to that in the ferroelectric state of the AFLC cell.

Further studies of the static and dynamic details of the h-chevron structure and its relation to the v chevron are necessary to reveal the mechanism of the stripe texture formation and to study the role of the layer ordering in the electro-optical response. The effects of the polarity and the asymmetry of the electric field on the layer stability are also of practical interest. Further experiments are now underway to clarify these problems.

ACKNOWLEDGMENTS

The authors would like to thank the staff of PF for their help during experiments. We wish to thank Professor K. Sekizawa, Professor Y. Takano, and Dr. K. Takase for their continuous encouragement during the study. This work was carried out under the approval of the Photon Factory Program Advisory Committee (Proposal Nos. 98G341 and 00G279). This work was partly supported by a Grant-In-Aid for Scientific Research on Priority Area (B) (Grant Nos. 2129202 and 12129206), the Ministry of Education, Science, Sports and Culture.

---

[1] N. A. Clark and S. T. Lagerwall, Appl. Phys. Lett. **36**, 899 (1980).
[2] S. T. Lagerwall, *Ferroelectric and Antiferroelectric Liquid Crystals* (Wiley, Weinheim, 1999).
[3] T. P. Rieker, N. A. Clark, G. S. S. Smith, D. S. Parmar, E. B. Sirota, and C. R. Safinya, Phys. Rev. Lett. **59**, 2658 (1987).
[4] N. Clark and T. P. Rieker, Phys. Rev. A **37**, 1053 (1988).
[5] N. A. Clark, T. P. Rieker, and J. E. Maclennan, Ferroelectrics **85**, 79 (1988).
[6] Y. Ouchi, H. Takano, H. Takezoe, and A. Fukuda, Jpn. J. Appl. Phys., Part 1 **27**, 1 (1988).
[7] H. Orihara, A. Suzuki, Y. Ishibashi, K. Gouhara, Y. Yamada, and N. Yamamoto, Jpn. J. Appl. Phys., Part 2 **28**, L676 (1989).
[8] Y. Sato, T. Tanaka, H. Kobayashi, K. Aoki, H. Watanabe, H. Takeshita, Y. Ouchi, H. Takezoe, and A. Fukuda, Jpn. J. Appl. Phys., Part 2 **28**, L483 (1989).
[9] M. Johno, Y. Ouchi, H. Takezoe, A. Fukuda, K. Terashima, and K. Furukawa, Jpn. J. Appl. Phys., Part 2 **29**, L111 (1990).
[10] K. Itoh, M. Johno, Y. Takanishi, Y. Ouchi, H. Takezoe, and A. Fukuda, Jpn. J. Appl. Phys., Part 1 **30**, 735 (1991).
[11] M. Oh-e, M. Isogai, and T. Kitamura, Liq. Cryst. **11**, 101 (1992).
[12] R. F. Shao, P. C. Willis, and N. A. Clark, Ferroelectrics **121**, 127 (1991).
[13] Y. Asao and T. Uchida, Jpn. J. Appl. Phys., Part 2 **32**, L604 (1993).
[14] A. G. Rappaport, P. A. Williams, B. N. Thomas, N. A. Clark, M. B. Ros, and D. M. Walba, Appl. Phys. Lett. **67**, 362 (1995).
[15] R. E. Geer, S. J. Singer, J. V. Selinger, B. R. Ratna, and R. Shashindhar, Phys. Rev. E **57**, 3059 (1998).
[16] L. S. Matkin, H. F. Gleeson, L. J. Baylils, S. J. Watson, N. Bowring, A. Seed, M. Hird, and J. W. Goodby, Appl. Phys. Lett. **77**, 340 (2000).
[17] S. J. Watson, L. S. Matkin, L. J. Baylis, N. Bowring, H. F. Gleeson, M. Hird, and J. Goodby, Phys. Rev. E **65**, 031705 (2002).
[18] P. Cluzeau, P. Barois, H. T. Nguyen, and C. Destrade, Eur. Phys. J. B **3**, 73 (1998).
[19] P. Cluzeau, P. Barois, and H. T. Nguyen, Eur. Phys. J. E **7**, 23 (2002).
[20] A. Iida, T. Noma, and H. Miyata, Jpn. J. Appl. Phys., Part 1 **35**, 160 (1996).
[21] A. Iida, T. Noma, and H. Miyata, Jpn. J. Appl. Phys., Part 1 **38**, 2845 (1999).
[22] A. Iida, T. Noma, and H. Miyata, Jpn. J. Appl. Phys., Part 1 **40**, 1345 (2000).
[23] Y. Takanishi, A. Iida, K. Ishikawa, H. Takezoe, and A. Fukuda, Jpn. J. Appl. Phys., Part 1 **35**, 683 (1996).
[24] Y. Takanishi, A. Iida, K. Ishikawa, H. Takezoe, and A. Fukuda, Jpn. J. Appl. Phys., Part 1 **38**, 4132 (1999).
[25] Y. Takanishi, T. Izumi, J. Watanabe, K. Ishikawa, H. Takezoe, and A. Iida, J. Mater. Chem. **9**, 2771 (1999).
[26] H. Gleeson and A. Mors, Liq. Cryst. **21**, 755 (1996).
[27] H. Gleeson, G. Bryant, and A. Morse, Mol. Cryst. Liq. Cryst. **362**, 203 (2001).
[28] Y. Takahashi, A. Iida, Y. Takanishi, T. Ogasawara, K. Ishikawa, and H. Takezoe, Jpn. J. Appl. Phys., Part 1 **40**, 3294 (2000).
[29] Y. Takahashi, A. Iida, Y. Takanishi, T. Ogasawara, K. Ishikawa, and H. Takezoe, Mol. Cryst. Liq. Cryst. **365**, 853 (2001).
[30] M. Johno, K. Ito, J. Lee, Y. Ouchi, H. Takezoe, A. Fukuda, and T. Kitazume, Jpn. J. Appl. Phys., Part 2 **29**, L107 (1990).